

Vorticity, kinetic energy, and suppressed gravitational wave production in strong first-order phase transitions

Daniel Cutting,^{1,2,*} Mark Hindmarsh,^{1,2,†} and David J. Weir^{2,3,‡}

¹*Department of Physics and Astronomy, University of Sussex, Falmer, Brighton BN1 9QH, U.K.*

²*Department of Physics and Helsinki Institute of Physics, PL 64, FI-00014 University of Helsinki, Finland*

³*School of Physics and Astronomy, University of Nottingham, Nottingham NG7 2RD, U.K.*

(Dated: July 21, 2020)

We have performed the first 3-dimensional simulations of strong first-order thermal phase transitions in the early Universe. For deflagrations, we find that the rotational component of the fluid velocity increases as the transition strength is increased. For detonations, however, the rotational velocity component remains constant and small. We also find that the efficiency with which kinetic energy is transferred to the fluid falls below theoretical expectations as we increase the transition strength. The probable origin of the kinetic energy deficit is the formation of reheated droplets of the metastable phase during the collision, slowing the bubble walls. The rate of increase in the gravitational wave energy density for deflagrations in strong transitions is suppressed compared to that predicted in earlier work. This is largely accounted for by the reduction in kinetic energy. Current modelling therefore substantially overestimates the gravitational wave signal for strong transitions with deflagrations, in the most extreme case by a factor of 10^3 . Detonations are less affected.

The Laser Interferometer Space Antenna (LISA), scheduled for launch in 2034, will open the mHz band of the emerging field of gravitational wave astronomy [1]. One of the most exciting goals of LISA is to probe the early universe by searching for gravitational wave signals from a first-order phase transition.

While the Standard Model is a cross-over [2, 3], there are many extensions with first-order phase transitions. These range from adding a scalar singlet [4–8] or doublet [9–11], to models with spontaneously broken conformal symmetry [12–18]. There are also models with phase transitions in hidden sectors [19–25]. Non-perturbative methods are sometimes necessary to establish the order of the phase transition [26–28].

An important parameter of a first-order phase transition is the trace anomaly difference, which quantifies the energy available for conversion to shear stress, and hence the power of the gravitational wave signal. If the trace anomaly difference is comparable to the radiation energy density of the universe, we call the transition ‘strong’. We denote the ratio of the trace anomaly to the thermal energy α , in which case a strong transition has $\alpha \sim 1$. We call $\alpha \gg 1$ ‘very strong’; our results do not access this region.

Substantial progress has been made in understanding gravitational wave production from first-order transitions with weak ($\alpha \sim 10^{-2}$) to intermediate ($\alpha \sim 10^{-1}$) strength using numerical simulations [29–32], as well as modelling [33–35]. While the fluid motion is well-described as a linear superposition of sound waves after a weak transition [29], rotational modes and turbulence are expected in stronger transitions [36, 37], which could substantially affect the gravitational wave signal [38–43].

At the same time, investigation of the underlying particle physics models indicates that intermediate to strong transitions are common in conservative extensions of the

Standard Model [44, 45], and very strong transitions are possible in models of composite Higgs and nearly conformal potentials [12–18]. It is also clear that LISA will be most likely to observe transitions where nonlinear effects like shocks and turbulence become important [32]. Recent work tackling the non-linear regime includes gravitational wave production from magnetohydrodynamic turbulence [46] and studies of shock collisions using a mixture of 1-dimensional simulations and modelling [47].

In this paper, we present results from the first numerical simulations of strong first-order phase transitions. We measure the fraction of the fluid kinetic energy in rotational modes, as traced by the mean-square velocity. As we increase the strength of the transition, this proportion grows substantially for deflagrations, with up to 65% of the mean square velocity found in rotational motion. The rotational proportion is far less for detonations, remaining roughly constant for all transition strengths.

As the transition strength α is increased, the efficiency of fluid kinetic energy production decreases below expectation. For deflagrations, this is associated with reduced wall speeds for expanding bubbles and reheating of the region in front of the walls, reducing the pressure difference [37, 48, 49]. The kinetic energy loss leads to a suppression in the gravitational wave power, by a factor which can be as small as $O(10^{-3})$. This means that current models substantially overestimate gravitational wave production from strong transitions with deflagrations. Detonations are less affected.

We model the phase transition with a real scalar field ϕ , coupled to a perfect fluid. We assume that there is no extra physics generating a magnetic field either before or during the phase transition. The model follows that used in previous work [31, 32, 50], differing by a change in the effective potential and therefore the equation of state. Our previous work used the high-temperature expansion

of the one-loop thermal effective potential, and we found that in stronger transitions, the total energy could drop below the scalar potential energy, which is unphysical. In this scenario, our algorithm would compute the temperature to be imaginary, causing a crash. Indeed, the high-temperature expansion is known to fail well below T_c ; for example, the speed of sound diverges and then becomes imaginary. To fix this we have introduced a simpler bag model equation of state, described below. The new equation of state changes only how the relevant thermodynamic parameters α and v_w are realised in terms of the parameters of the potential and field-fluid coupling term. The flows around the expanding bubbles, and hence the gravitational wave spectrum, depend on the underlying theory only through α and the wall speed v_w , with the overall frequency scale set by the redshifted mean bubble separation.

Our coupled field-fluid system has energy-momentum tensor

$$T^{\mu\nu} = \partial^\mu \phi \partial^\nu \phi - \frac{1}{2} g^{\mu\nu} (\partial\phi)^2 + (\epsilon + p) U^\mu U^\nu + g^{\mu\nu} p \quad (1)$$

where $U = \gamma(1, \mathbf{v})$, with fluid 3-velocity \mathbf{v} and associated Lorentz factor γ . The internal energy ϵ and pressure p are

$$\epsilon = 3a(\phi)T^4 + V_0(\phi), \quad p = a(\phi)T^4 - V_0(\phi), \quad (2)$$

and the enthalpy is $w = \epsilon + p$.

The zero-temperature effective potential is

$$V_0(\phi) = \frac{1}{2} M^2 \phi^2 - \frac{1}{3} \mu \phi^3 + \frac{1}{4} \lambda \phi^4 - V_c, \quad (3)$$

where V_c is chosen such that $V_0(\phi_b) = 0$, and ϕ_b is the value of ϕ in the broken phase at $T = 0$. We denote the potential energy difference between the vacua by $\Delta V_0 = V_0(0) - V_0(\phi_b)$.

We write the thermal effective potential of our bag model as

$$V(\phi, T) = V_0(\phi) - T^4 (a(\phi) - a_0), \quad (4)$$

where $a(\phi)$ models the change in degrees of freedom during the transition. We take

$$a(\phi) = a_0 - \frac{\Delta V_0}{T_c^4} \left[3 \left(\frac{\phi}{\phi_b} \right)^2 - 2 \left(\frac{\phi}{\phi_b} \right)^3 \right], \quad (5)$$

where $a_0 = (\pi^2/90)g_*$ with g_* the effective number of relativistic degrees of freedom in the symmetric phase. Both $\phi = 0$ and $\phi = \phi_b$ are stationary points of the function for all T . For our choice of $a(\phi)$ the minima of V become degenerate at $T = T_c$, as required.

The energy-momentum tensor can be decomposed into field and fluid parts, coupled through a friction term,

$$\partial_\mu T_\phi^{\mu\nu} = -\partial_\mu T_f^{\mu\nu} = \eta U^\mu \partial_\mu \phi \partial^\nu \phi. \quad (6)$$

Ref. [32] used a field- and temperature-dependent friction parameter $\eta = \tilde{\eta} \phi^2 / T$. Although this models high temperature physics more accurately [51], strong transitions can reach small temperatures and again the high-temperature approximation fails. With small temperatures we also find numerical instabilities and so revert to using a constant η .

The phase transition strength is parametrised by the trace anomaly difference

$$\Delta\theta(T) = \frac{1}{4} \frac{d}{dT} \Delta V - \Delta V, \quad (7)$$

where $\Delta V = V(0, T) - V(\phi_b, T)$. The strength parameter is then

$$\alpha = \Delta\theta(T_n) / \epsilon_r(T_n). \quad (8)$$

where T_n is the nucleation temperature and $\epsilon_r = 3w/4$ the radiation energy density.

We assume that the duration of the phase transition is much less than the Hubble time H_n^{-1} , and neglect the effect of expansion. This is comparable to the statement that $H_n R_* \ll 1$, where R_* is the mean bubble separation. In this regime the contribution of bubble collisions to the gravitational wave signal is negligible. To neglect expansion the final simulation time t_{fin} must also be much smaller than H_n^{-1} . For all our simulations $t_{\text{fin}} \leq 10 R_*$.

The mean gravitational wave energy density is

$$\rho_{\text{gw}} = \frac{1}{32\pi G} \frac{1}{\mathcal{V}} \int_{\mathcal{V}} d^3x \overline{h_{ij}^{\text{TT}} \dot{h}_{ij}^{\text{TT}}}, \quad (9)$$

where \mathcal{V} is the simulation volume, h_{ij}^{TT} is the transverse traceless metric perturbation and the line indicates averaging over a characteristic period of the gravitational waves. We find h_{ij}^{TT} in Fourier space by a standard technique [29, 31, 52], sourced only by the fluid, the dominant contribution when $\alpha \lesssim 1$ and $H_n R_* \ll 1$ [29, 31, 32].

We express the gravitational wave energy density in terms of the parameter $\Omega_{\text{gw}} = \rho_{\text{gw}} / \rho_c$, with ρ_c the critical energy density. Our assumptions on α and $H_n R_*$ ensure that $\Omega_{\text{gw}} \ll 1$ at all times. They also ensure that the gravitational backreaction is negligible compared to the pressure forces, as the wavelength of the density perturbations $\sim R_*$ is much less than the Jeans length $\sim c_s / H_n \sqrt{\delta}$, where δ is the energy density contrast averaged over the wavelength being considered¹. We leave a deeper analysis of gravitational backreaction in the case $H_n R_* \sim c_s / \sqrt{\delta}$ to a later study.

¹ For the parameter space we consider, we determined that the variation of the energy density is at most a factor of twenty in the asymptotic fluid profile that develops around an expanding bubble; δ will be less than this due to averaging over a given wavelength.

We perform a series of three-dimensional simulations of the field-fluid system. The simulation code is the same as used in Ref. [32] except for the above changes.

We scan over α for three subsonic deflagrations with asymptotic wall speeds $v_w = \{0.24, 0.44, 0.56\}$, and two detonations with $v_w = \{0.82, 0.92\}$. The asymptotic wall speeds, and their fluid profiles, are found with a spherically symmetric version of the code [31, 32, 53, 54], run with the same parameters until $t = 10000T_c^{-1}$. As we increase α , the maximum velocity of the asymptotic fluid profile v_p increases. For each v_w , there is a maximum v_p , and hence a maximum strength α_{\max} , above which solutions either do not exist (subsonic deflagrations), or change into hybrids. We do not consider hybrids here.

The values of η needed for these wall speeds are given in the supplemental material. By comparison, the Standard Model estimate is $\eta \simeq 3\phi_b^2/T_c$ [51, 55, 56].

All simulations have the number of bubbles $N_b = 8$, lattice spacing $\delta x = 1.0T_c^{-1}$, timestep $\delta t = 0.2T_c^{-1}$, and $L^3 = 960^3$ lattice sites, giving a mean bubble separation $R_* = L\delta x/N_b^{1/3} = 480T_c^{-1}$. All bubbles are nucleated simultaneously with a gaussian profile at the same locations at the start of each simulation. The initial profile of the bubbles is insignificant as they approach the same asymptotic profile.

We fix $g_* = 106.75$, $M^2 = 0.0427T_c^2$, $\mu = 0.168T_c$ and $\lambda = 0.0732$, in turn fixing $\phi_b = 2.0T_c$. This sets the relative change in degrees of freedom to $[a(\phi_b) - a_0]/a_0 = 5.9 \times 10^{-3}$. To change the transition strength we vary T_n .

We output slices of the temperature T , fluid speed v and vorticity magnitude $|\nabla \times \mathbf{v}|$. Movies created from these slices are available at [57]. Selected stills are included in the supplemental material.

We measure the RMS fluid 3-velocity \bar{v} , and its irrotational and rotational parts \bar{v}_{\parallel} and \bar{v}_{\perp} . We also track the enthalpy-weighted RMS four-velocity \bar{U}_f defined as

$$\bar{U}_f^2 = \frac{1}{\bar{w}\mathcal{V}} \int_{\mathcal{V}} d^3x w \gamma^2 v^2, \quad (10)$$

where \bar{w} the mean enthalpy density. This gives an indication of the magnitude of the shear stress, the source of gravitational waves.

A similar quantity \bar{U}_{ϕ} can be constructed to track the progress of the phase transition

$$\bar{U}_{\phi}^2 = \frac{1}{\bar{w}\mathcal{V}} \int_{\mathcal{V}} d^3x \partial_i \phi \partial_i \phi, \quad (11)$$

proportional to the total area of the phase boundary. We call the time when \bar{U}_{ϕ} reaches its maximum the peak collision time, t_{pc} . Note that $t_{pc} \propto R_*/v_w$. To see how these global quantities evolve during a detonation and a deflagration see Fig. 10 in the supplemental material.

To check the dependence of our key observables on lattice spacing, we perform simulations with the same physical volume and various lattice spacings $\delta x T_c =$

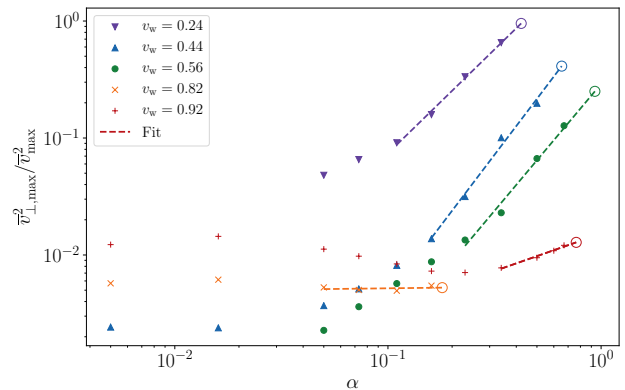


FIG. 1. Proportion of mean square fluid velocity in the rotational modes. We plot the ratio of $\bar{v}_{\perp, \max}$ to \bar{v}_{\max} against α . Dashed lines give a linear fit for the last four simulation points. The fits are extrapolated to α_{\max} for deflagrations, or to the largest α for which a wall speed corresponds to a detonation (hollow circles).

$\{2.0, 1.5, 1.0, 0.75, 0.5\}$ for $v_w = 0.24$ and $v_w = 0.92$ and $\alpha = 0.5$. We find that $\bar{v}_{\perp, \max}^2$, $\bar{U}_{f, \max}$, and Ω_{gw} converge with lattice spacing. We perform a quadratic fit with δx for each quantity, finding that $\bar{U}_{f, \max}$ and Ω_{gw} differ from the continuum limit by $O(1\%)$. The quantity that is most sensitive to the grid is $\bar{v}_{\perp, \max}^2$ which we underestimate from the continuum limit by $\simeq 25\%$. We also test convergence of key observables with timestep, finding in all cases that convergence is better for δt than for δx . It is important to check how close the colliding bubbles are to their asymptotic profile. We find that spherically symmetric bubbles with diameter R_c have at worst \bar{U}_f within 20% of the asymptotic \bar{U}_f . In the supplemental material we show our convergence test results and the deviation from asymptotic \bar{U}_f for all v_w and α considered here.

From our simulations we see that a rotational component of velocity is generated during the bubble collision phase. In order to gauge the relative amount of kinetic energy in the rotational component of velocity, we consider the ratio of the maxima of mean square 3-velocities $\bar{v}_{\perp, \max}^2 / \bar{v}_{\max}^2$. We plot this in Fig. 1. As we increase α for the deflagrations, we see that the proportion of the velocity found in rotational modes increases dramatically, whereas for detonations it stays constant. The deflagrations with smaller wall velocities have a larger proportion of the velocity in rotational modes. For $v_w = 0.24$, $\alpha = 0.34$ the ratio $\bar{v}_{\perp, \max}^2 / \bar{v}_{\max}^2 = 0.65$, and if we naively extrapolate the trend in the last few points up to α_{\max} this increases to 0.95.

Fig. 11 of the supplemental material shows that the vorticity is generated inside the bubbles, not outside where the fluid shells first interact.

To better understand transfer of energy from the scalar field to the fluid, we plot how \bar{U}_{ϕ} and \bar{U}_f change as we

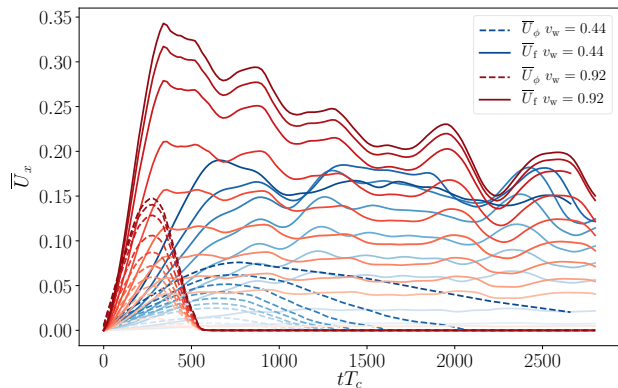


FIG. 2. The evolution of \bar{U}_ϕ (dashed lines) and \bar{U}_f (solid lines) for simulations with increasing α (darker shades). In blue we show deflagrations with $v_w = 0.44$ whereas red lines show detonations with $v_w = 0.92$.

increase α for detonations with $v_w = 0.92$ and deflagrations with $v_w = 0.44$ (Fig. 2). When \bar{U}_ϕ reaches its maximum, the volumes in each phase are approximately equal. As the phase boundary sweeps out the remaining regions of metastable phase, \bar{U}_ϕ relaxes to zero. It is striking that for deflagrations the relaxation takes longer as we increase α , whereas for detonations the shape of \bar{U}_ϕ remains unchanged. The phase boundaries in a deflagration must therefore move more slowly in the later stages, as the transition strength increases.

The reason for the slowing is that the metastable phase is reheated by the fluid shells in front of the bubble walls [37, 48, 49]. Towards the end of the transition the remaining metastable phase forms into hot droplets (see Fig. 11 in the supplemental material). The higher pressure inside the droplets opposes their collapse.

For detonations, where the fluid shell develops behind the bubble wall, shrinking regions of the metastable phase are not reheated (see Fig. 12 in the supplemental material).

Fig. 2 also shows that \bar{U}_f increases with α , as one expects from the increasing scalar potential energy. However, the maximum is below that expected from a single bubble, which is a good estimate of \bar{U}_f at low α [31, 32].

To obtain the single-bubble estimate, simulations of expanding spherical bubbles are performed, and the expected enthalpy-weighted RMS velocity $\bar{U}_{f,\text{exp}}$ is that of the fluid shell when the wall reaches a diameter of R_* . We then take the ratio with the maximum of \bar{U}_f in each simulation, shown in Fig. 3. Note that due to finite volume effects \bar{U}_f oscillates in our simulations, giving an $O(10\%)$ uncertainty to this estimate.

For all wall speeds, the ratio of $\bar{U}_{f,\text{max}}$ to $\bar{U}_{f,\text{exp}}$ decreases as we increase the transition strength. However, for deflagrations the decrease in the kinetic efficiency is more dramatic, and more rapid for slower walls: in the

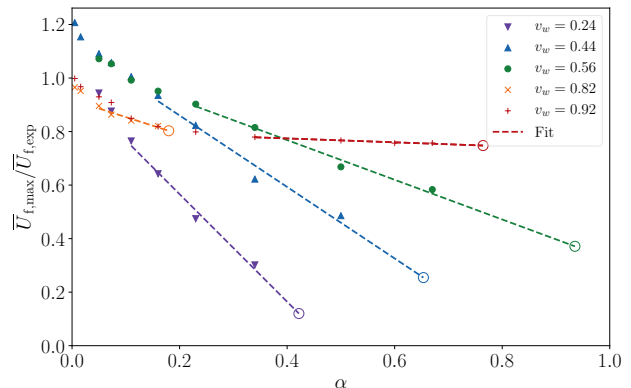


FIG. 3. Comparison between the maximum value of \bar{U}_f in each simulation and that predicted by [58] for the given v_w and α . Dashed lines give a linear fit for the last four simulation points. Hollow circles show the extrapolation to α_{max} for deflagrations, or up to the largest α for which the wall speed corresponds to a detonation.

slowest deflagration ($v_w = 0.24$), $\bar{U}_{f,\text{max}}/\bar{U}_{f,\text{exp}}$ reaches 0.3. The decrease is approximately linear; a naive linear extrapolation to the maximum possible strength is indicated by open circles. The loss of kinetic energy is probably a result of the slowing discussed above, limiting the transfer of energy.

The deficit in kinetic energy can be expected to reduce the gravitational wave signal. In current modelling [32, 59], the expected gravitational wave density parameter from a flow with $\bar{U}_{f,\text{exp}}$ at time $t \ll H_n^{-1}$ is

$$\Omega_{\text{gw},\text{exp}} = 3\tilde{\Omega}_{\text{gw}} \left(\frac{\bar{w}}{\bar{\epsilon}}\right)^2 \bar{U}_{f,\text{exp}}^4 (H_n t)(H_n R_*), \quad (12)$$

where $\tilde{\Omega}_{\text{gw}}$ has been shown to be a constant of $O(10^{-2})$ in weak and intermediate transitions. Here, we take $\tilde{\Omega}_{\text{gw}} = 10^{-2}$. In Fig. 4 we plot the ratio of Ω_{gw}/t to $\Omega_{\text{gw},\text{exp}}/t$, where Ω_{gw}/t is averaged over the final $\Delta t = 2R_*$ of the simulation. In the most extreme case, $v_w = 0.24$ and $\alpha = 0.34$, the ratio is 2×10^{-3} . This is even less than the kinetic energy suppression suggests, a factor of $(\bar{U}_{f,\text{max}}/\bar{U}_{f,\text{exp}})^4 \simeq 8 \times 10^{-3}$.

A table of simulation parameters and measured quantities can be found in the supplemental material.

We have performed the first 3-dimensional simulations of strong first-order phase transitions, with the strength parameter α up to an order of magnitude larger than those previously studied [32].

A rotational component of velocity \bar{v}_\perp is generated during the collision phase. For deflagrations, the ratio $\bar{v}_{\perp,\text{max}}^2/\bar{v}_{\text{max}}^2$ grows rapidly with α , reaching 0.65 for $v_w = 0.24$. For detonations, the ratio is $O(10^{-2})$ —showing no consistent trend with α .

For stronger phase transitions a smaller proportion of the scalar potential energy is transferred into fluid kinetic

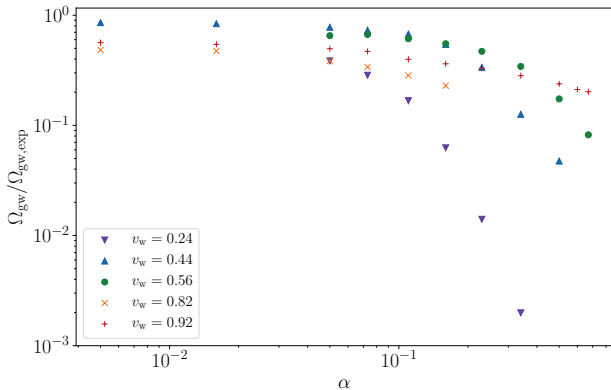


FIG. 4. Comparison of the gravitational waves produced in our simulations against that predicted by Eq. (12) using $\bar{U}_{f,exp}$ found from v_w and α .

energy than is expected from the behaviour of isolated bubbles. For deflagrations, we suppose that the deficit is due to reheating of the metastable phase slowing the bubble walls during the collision phase. The deficit can be substantial, with $\bar{U}_{f,max}/\bar{U}_{f,exp}$ falling to ~ 0.3 for $v_w = 0.24$ in our simulations, and could fall as low as 0.1 using a naive linear extrapolation to the maximum possible strength at that wall speed.

The gravitational wave intensity is lower than expected, by a factor of order 10^{-3} for the strongest deflagration with the lowest wall speed. This can mostly be accounted for by the kinetic energy deficit. Detonations do not suffer such a dramatic suppression, with the smallest suppression factor about 0.2 for $v_w = 0.92$.

Our results have important consequences for gravitational waves from phase transitions. They indicate that the current model [32, 59] overestimates the gravitational wave power spectrum for strong transitions, by a factor of a few for detonations, and by an order of magnitude or more for deflagrations. We estimate² that to obtain a signal to noise ratio of $10 \bar{U}_f$ must be at least 0.07. Therefore the kinetic energy suppression we observe will probably render transitions with $v_w = 0.24$ unobservable except for within a very small region of parameter space. Faster walls suffer less suppression, though the observable parameter space is still reduced.

We plan larger simulations to characterise more precisely the suppression, and its effect on observability.

The authors would like to thank Chiara Caprini, Kari Rummukainen, and Danièle Steer for helpful discussions.

² We use PTPlot v1.01, [http://www.ptplot.org/ptplot/\[? \]](http://www.ptplot.org/ptplot/[?]), to compute and plot signal to noise ratio (SNR) curves from first-order phase transitions for LISA. We choose $g_* = 106.75$ and an optimistic $T_n = 100$ GeV. The resulting plot shows that an SNR of 10 requires \bar{U}_f of at least 0.07 for all $H_n R_*$.

Our simulations made use of the resources of the Finnish Centre for Scientific Computing CSC. DC (ORCID ID 0000-0002-7395-7802) is supported by an STFC Studentship. MH (ORCID ID 0000-0002-9307-437X) acknowledges support from the Science and Technology Facilities Council, grant no. ST/P000819/1. DJW (ORCID ID 0000-0001-6986-0517) is supported by a Science and Technology Facilities Council Ernest Rutherford Fellowship, grant no. ST/R003904/1, by the Research Funds of the University of Helsinki, and by the Academy of Finland, grant no. 286769.

* d.cutting@sussex.ac.uk

† m.b.hindmarsh@sussex.ac.uk

‡ david.weir@nottingham.ac.uk

- [1] H. Audley et al., (2017), arXiv:1702.00786 [astro-ph.IM].
- [2] K. Kajantie, M. Laine, K. Rummukainen, and M. E. Shaposhnikov, Phys.Rev.Lett. **77**, 2887 (1996), arXiv:hep-ph/9605288 [hep-ph].
- [3] K. Kajantie, M. Laine, K. Rummukainen, and M. E. Shaposhnikov, Nucl.Phys. **B493**, 413 (1997), arXiv:hep-lat/9612006 [hep-lat].
- [4] S. Profumo, M. J. Ramsey-Musolf, and G. Shaughnessy, JHEP **08**, 010 (2007), arXiv:0705.2425 [hep-ph].
- [5] J. R. Espinosa, T. Konstandin, and F. Riva, Nucl. Phys. **B854**, 592 (2012), arXiv:1107.5441 [hep-ph].
- [6] J. M. Cline and K. Kainulainen, JCAP **1301**, 012 (2013), arXiv:1210.4196 [hep-ph].
- [7] S. Profumo, M. J. Ramsey-Musolf, C. L. Wainwright, and P. Winslow, Phys. Rev. **D91**, 035018 (2015), arXiv:1407.5342 [hep-ph].
- [8] A. Beniwal, M. Lewicki, M. White, and A. G. Williams, JHEP **02**, 183 (2019), arXiv:1810.02380 [hep-ph].
- [9] M. Kakizaki, S. Kanemura, and T. Matsui, Phys. Rev. **D92**, 115007 (2015), arXiv:1509.08394 [hep-ph].
- [10] G. C. Dorsch, S. J. Huber, T. Konstandin, and J. M. No, JCAP **1705**, 052 (2017), arXiv:1611.05874 [hep-ph].
- [11] P. Basler, M. Krause, M. Muhlleitner, J. Wittbrodt, and A. Wlotzka, JHEP **02**, 121 (2017), arXiv:1612.04086 [hep-ph].
- [12] L. Randall and G. Servant, JHEP **05**, 054 (2007), arXiv:hep-ph/0607158 [hep-ph].
- [13] T. Konstandin, G. Nardini, and M. Quiros, Phys. Rev. **D82**, 083513 (2010).
- [14] T. Konstandin and G. Servant, JCAP **1112**, 009 (2011), arXiv:1104.4791 [hep-ph].
- [15] B. von Harling and G. Servant, JHEP **01**, 159 (2018), arXiv:1711.11554 [hep-ph].
- [16] B. M. Dillon, B. K. El-Menoufi, S. J. Huber, and J. P. Manuel, Phys. Rev. **D98**, 086005 (2018), arXiv:1708.02953 [hep-th].
- [17] E. Megías, G. Nardini, and M. Quirós, JHEP **09**, 095 (2018), arXiv:1806.04877 [hep-ph].
- [18] S. Bruggisser, B. Von Harling, O. Matsedonskyi, and G. Servant, JHEP **12**, 099 (2018), arXiv:1804.07314 [hep-ph].
- [19] P. Schwaller, Phys. Rev. Lett. **115**, 181101 (2015), arXiv:1504.07263 [hep-ph].
- [20] A. Addazi and A. Marciano, Chin. Phys. **C42**, 023107

- (2018), arXiv:1703.03248 [hep-ph].
- [21] M. Aoki, H. Goto, and J. Kubo, Phys. Rev. **D96**, 075045 (2017), arXiv:1709.07572 [hep-ph].
- [22] D. Croon, V. Sanz, and G. White, JHEP **08**, 203 (2018), arXiv:1806.02332 [hep-ph].
- [23] M. Breitbach, J. Kopp, E. Madge, T. Opferkuch, and P. Schwaller, (2018), arXiv:1811.11175 [hep-ph].
- [24] N. Okada and O. Seto, Phys. Rev. **D98**, 063532 (2018), arXiv:1807.00336 [hep-ph].
- [25] T. Hasegawa, N. Okada, and O. Seto, Phys. Rev. **D99**, 095039 (2019), arXiv:1904.03020 [hep-ph].
- [26] T. Gorda, A. Helset, L. Niemi, T. V. I. Tenkanen, and D. J. Weir, JHEP **02**, 081 (2019), arXiv:1802.05056 [hep-ph].
- [27] O. Gould, J. Kozaczuk, L. Niemi, M. J. Ramsey-Musolf, T. V. I. Tenkanen, and D. J. Weir, (2019), arXiv:1903.11604 [hep-ph].
- [28] K. Kainulainen, V. Keus, L. Niemi, K. Rummukainen, T. V. I. Tenkanen, and V. Vaskonen, (2019), arXiv:1904.01329 [hep-ph].
- [29] M. Hindmarsh, S. J. Huber, K. Rummukainen, and D. J. Weir, Phys.Rev.Lett. **112**, 041301 (2014), arXiv:1304.2433 [hep-ph].
- [30] J. T. Giblin and J. B. Mertens, Phys.Rev. **D90**, 023532 (2014), arXiv:1405.4005 [astro-ph.CO].
- [31] M. Hindmarsh, S. J. Huber, K. Rummukainen, and D. J. Weir, Phys. Rev. **D92**, 123009 (2015), arXiv:1504.03291 [astro-ph.CO].
- [32] M. Hindmarsh, S. J. Huber, K. Rummukainen, and D. J. Weir, Phys. Rev. **D96**, 103520 (2017), arXiv:1704.05871 [astro-ph.CO].
- [33] M. Hindmarsh, Phys. Rev. Lett. **120**, 071301 (2018), arXiv:1608.04735 [astro-ph.CO].
- [34] R. Jinno and M. Takimoto, Phys. Rev. **D95**, 024009 (2017), arXiv:1605.01403 [astro-ph.CO].
- [35] T. Konstandin, JCAP **1803**, 047 (2018), arXiv:1712.06869 [astro-ph.CO].
- [36] E. Witten, Phys.Rev. **D30**, 272 (1984).
- [37] H. Kurki-Suonio, Nucl.Phys. **B255**, 231 (1985).
- [38] M. Kamionkowski, A. Kosowsky, and M. S. Turner, Phys.Rev. **D49**, 2837 (1994), arXiv:astro-ph/9310044 [astro-ph].
- [39] C. Caprini, R. Durrer, and G. Servant, Phys.Rev. **D77**, 124015 (2008), arXiv:0711.2593 [astro-ph].
- [40] G. Gogoberidze, T. Kahniashvili, and A. Kosowsky, Phys.Rev. **D76**, 083002 (2007), arXiv:0705.1733 [astro-ph].
- [41] C. Caprini, R. Durrer, and G. Servant, JCAP **0912**, 024 (2009), arXiv:0909.0622 [astro-ph.CO].
- [42] C. Caprini, R. Durrer, T. Konstandin, and G. Servant, Phys.Rev. **D79**, 083519 (2009), arXiv:0901.1661 [astro-ph.CO].
- [43] P. Niksa, M. Schlexer, and G. Sigl, Class. Quant. Grav. **35**, 144001 (2018), arXiv:1803.02271 [astro-ph.CO].
- [44] J. Ellis, M. Lewicki, and J. M. No, (2018), 10.1088/1475-7516/2019/04/003, [JCAP1904,003(2019)], arXiv:1809.08242 [hep-ph].
- [45] J. Ellis, M. Lewicki, J. M. No, and V. Vaskonen, (2019), arXiv:1903.09642 [hep-ph].
- [46] A. R. Pol, S. Mandal, A. Brandenburg, T. Kahniashvili, and A. Kosowsky, (2019), arXiv:1903.08585 [astro-ph.CO].
- [47] R. Jinno, H. Seong, M. Takimoto, and C. M. Um, (2019), arXiv:1905.00899 [astro-ph.CO].
- [48] T. Konstandin and J. M. No, JCAP **1102**, 008 (2011), arXiv:1011.3735 [hep-ph].
- [49] A. Mégevand and S. Ramírez, Nucl. Phys. **B928**, 38 (2018), arXiv:1710.06279 [astro-ph.CO].
- [50] J. Ignatius, K. Kajantie, H. Kurki-Suonio, and M. Laine, Phys.Rev. **D49**, 3854 (1994), arXiv:astro-ph/9309059 [astro-ph].
- [51] B.-H. Liu, L. D. McLerran, and N. Turok, Phys. Rev. **D46**, 2668 (1992).
- [52] J. Garcia-Bellido, D. G. Figueroa, and A. Sastre, Phys.Rev. **D77**, 043517 (2008), arXiv:0707.0839 [hep-ph].
- [53] H. Kurki-Suonio and M. Laine, Phys.Rev. **D54**, 7163 (1996), arXiv:hep-ph/9512202 [hep-ph].
- [54] H. Kurki-Suonio and M. Laine, Phys.Rev. **D51**, 5431 (1995), arXiv:hep-ph/9501216 [hep-ph].
- [55] P. John and M. G. Schmidt, Nucl. Phys. **B598**, 291 (2001), [Erratum: Nucl. Phys.B648,449(2003)], arXiv:hep-ph/0002050 [hep-ph].
- [56] G. D. Moore and T. Prokopec, Phys.Rev. **D52**, 7182 (1995), arXiv:hep-ph/9506475 [hep-ph].
- [57] D. Cutting, (2019), see movies of strong phase transitions available at <https://vimeo.com/album/5968055>.
- [58] J. R. Espinosa, T. Konstandin, J. M. No, and G. Servant, JCAP **1006**, 028 (2010), arXiv:1004.4187 [hep-ph].
- [59] C. Caprini et al., JCAP **1604**, 001 (2016), arXiv:1512.06239 [astro-ph.CO].

SUPPLEMENTAL MATERIAL

Field and fluid equations of motion

In order to obtain the equations of motion for our field and fluid system we focus on the coupling between the field and fluid parts of our energy momentum tensor. The current of the energy-momentum tensor can be split into field and fluid parts and coupled through a dissipative friction term,

$$[\partial_\mu T^{\mu\nu}]_{\text{field}} = (\partial_\mu \partial^\mu \phi) \partial^\nu \phi - \frac{\partial V}{\partial \phi} \partial^\nu \phi = \delta^\nu, \quad (13)$$

$$[\partial_\mu T^{\mu\nu}]_{\text{fluid}} = \partial_\mu [(\epsilon + p)U^\mu U^\nu] + \partial^\nu p + \frac{\partial V}{\partial \phi} \partial^\nu \phi = -\delta^\nu. \quad (14)$$

We can then write this coupling term as

$$\delta^\nu = \eta U^\mu \partial_\mu \phi \partial^\nu \phi. \quad (15)$$

From these two equations we can extract the equation of motion for our system. By taking Eq (13) and dividing through by $\delta^\nu \phi$ we obtain

$$-\ddot{\phi} + \nabla^2 \phi - \frac{\partial V}{\partial \phi} = \eta \gamma (\dot{\phi} + v^i \partial_i \phi). \quad (16)$$

We find the equation of motion for the fluid energy density $E = \gamma \epsilon$ by contracting Eq (14) with U_ν giving

$$\begin{aligned} \dot{E} + \partial_i (E v^i) + p[\dot{\gamma} + \partial(\gamma v^i)] - \frac{\partial V}{\partial \phi} \gamma (\dot{\phi} + v^i \partial_i \phi) \\ = \eta \gamma^2 (\dot{\phi} + v^i \partial_i \phi)^2. \end{aligned} \quad (17)$$

Finally we obtain an expression for the fluid momentum density $Z_i = \gamma(\epsilon + p)U_i$ by considering the spatial components of Eq (14),

$$\dot{Z} + \partial_j (Z_i v^j) + \partial_i p + \frac{\partial V}{\partial \phi} \partial_i \phi = -\eta \gamma (\dot{\phi} + v^j \partial_j \phi) \partial_i \phi. \quad (18)$$

Gravitational waves

To obtain the gravitational wave energy density we must first calculate the transverse traceless perturbations in the metric, h_{ij}^{TT} . We operate in linearised gravity and therefore the equation of motion for h_{ij}^{TT} is

$$\square h_{ij}^{TT} = 16\pi G T_{ij}^{TT}, \quad (19)$$

where T_{ij}^{TT} is the transverse traceless projection of the energy-momentum tensor.

Due to the numerical cost of computing the transverse traceless components of the energy-momentum tensor, it is useful to instead track an auxiliary tensor u_{ij} [52] which evolves according to

$$\square u_{ij} = 16\pi G T_{ij}. \quad (20)$$

Then to obtain h_{ij}^{TT} from u_{ij} we apply the transverse traceless projector in wave space,

$$\tilde{h}_{ij}^{TT}(\mathbf{k}, t) = \Lambda_{ij,lm}(\mathbf{k}) \tilde{u}_{lm}(\mathbf{k}, t), \quad (21)$$

where

$$\Lambda_{ij,lm}(\mathbf{k}) = P_{im}(\mathbf{k}) P_{jl}(\mathbf{k}) - \frac{1}{2} P_{ij}(\mathbf{k}) P_{lm}(\mathbf{k}), \quad (22)$$

and

$$P_{ij}(\mathbf{k}) = \delta_{ij} - \hat{k}_i \hat{k}_j. \quad (23)$$

This method then allows us to only need to perform the necessary Fourier transforms and projections to calculate the gravitational wave energy density at regular intervals rather than every timestep.

Resolution convergence

To ensure the validity of our simulations we performed a series of lattice resolution checks. To do this we repeated two simulations with $v_w = 0.44$ and $v_w = 0.92$ and $\alpha = 0.5$ for a variety of different lattice spacings and timesteps while keeping the total physical volume and duration of the simulations fixed. We plot the convergence of several key quantities with δx in Fig. 5 through Fig. 7. We also plot a quadratic fit for the convergence of each quantity with δx . We can see that all quantities converge. The worst convergence is for $\bar{v}_{\perp, \text{max}}^2$ which for $\delta x = 1.0 T_c^{-1}$ we underestimate by up to 25% from the extrapolation to the continuum limit. We also performed tests for convergence of our simulations with δt . For $\delta t = 0.2 T_c^{-1}$ the error from our simulations is within $\sim 1\%$ from the continuum limit for $(\bar{\Omega}_{\text{gw}}/H_n t)(1/H_n R_c)$ and $\bar{U}_{\text{f,max}}$ and $\sim 5\%$ for $\bar{v}_{\perp, \text{max}}^2$.

Convergence to asymptotic fluid flow

In addition to testing convergence with lattice spacing, we also check how close the fluid shells around colliding bubbles in our simulation are to the final asymptotic profiles. To do this we perform spherically symmetric 1D simulations of isolated bubbles and calculate $\bar{U}_{\text{f,exp}}$ from the fluid shell when the bubble has diameter R_c . We then compare this to $\bar{U}_{\text{f,exp}}$ calculated from the fluid shell at $t = 10000 T_c^{-1}$, i.e when the diameter is $\gg R_c$ and the profile has reached its asymptotic solution. We plot the

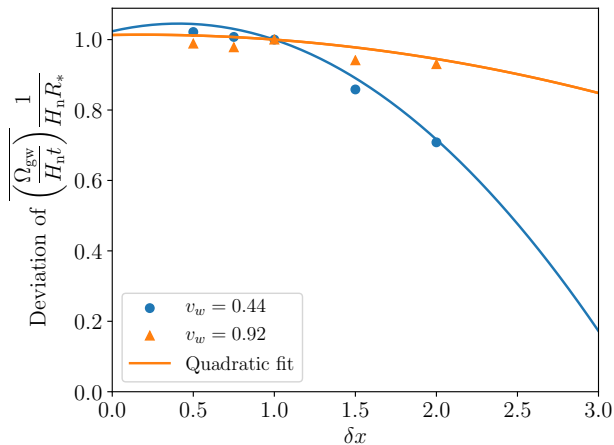


FIG. 5. Variation of gravitational wave energy density with δx for $v_w = 0.44$ and $v_w = 0.92$ and transition strength of $\alpha = 0.5$. We normalise the y -axis by dividing by the result from the simulation presented in the paper ($\delta x = 1.0$). Note that $(\overline{\Omega_{\text{gw}}}/H_n t)$ signifies that we average the quantity inside the brackets over the final $\Delta t = 2R_*$ of the simulation.

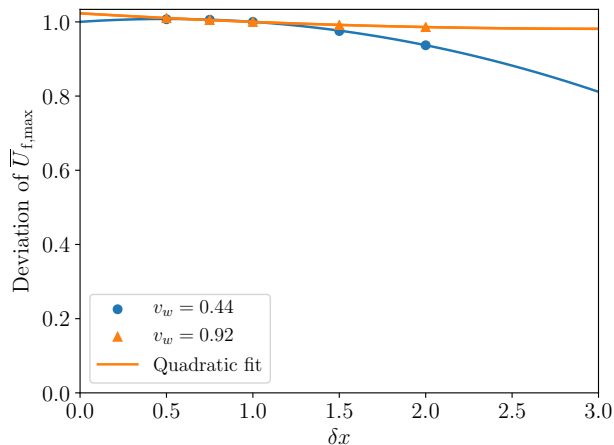


FIG. 6. Variation of $\overline{U}_{f,\text{max}}$ with δx for $v_w = 0.44$ and $v_w = 0.92$ and transition strength of $\alpha = 0.5$. We normalise the y -axis by dividing by the result from the simulation presented in the paper ($\delta x = 1.0$).

ratio of these two quantities for all α and v_w in Fig. 8. We can see that the bubbles colliding with the diameter of the average bubble separation are within 20% of the asymptotic \overline{U}_f for all simulations. We believe this to be sufficient for this study, and save a further investigation on the convergence with increasing R_c for a future work.

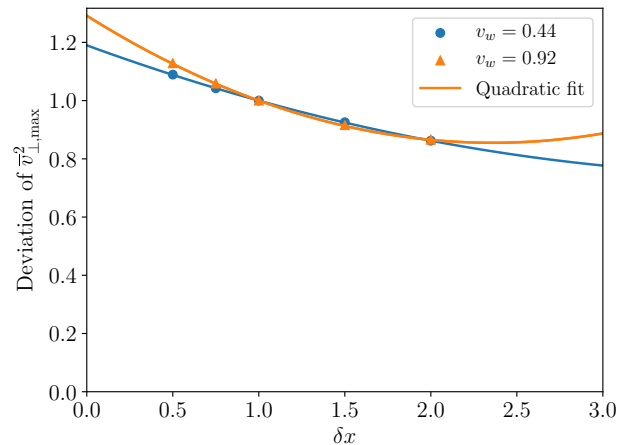


FIG. 7. Variation of $\overline{v}_{\perp,\text{max}}$ with δx for $v_w = 0.44$ and $v_w = 0.92$ and transition strength of $\alpha = 0.5$. We normalise the y -axis by dividing by the result from the simulation presented in the paper ($\delta x = 1.0$).

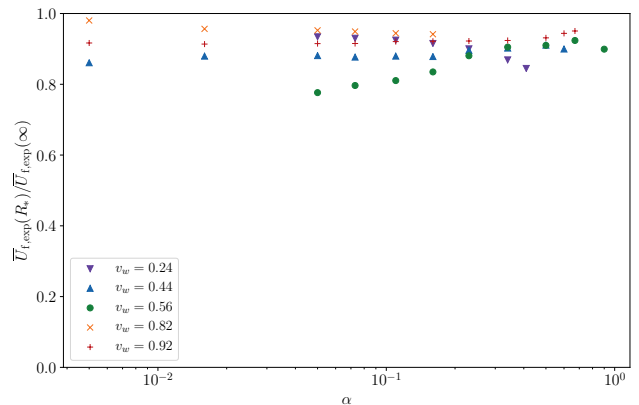


FIG. 8. Plot comparing $\overline{U}_{f,\text{exp}}$ calculated for an isolated bubble when the diameter of the bubble is R_* to late times ($t = 10000 T_c^{-1}$) where it has reached the asymptotic profile.

Parameter space

In order to understand the regions of parameter space mapped out by our simulations, it can be illuminating to plot the asymptotic maximum fluid flow velocity v_p against the wall velocity v_w for each simulation point. We do this in Fig. 9. Plotting the parameter space in this manner separates subsonic-deflagrations, supersonic-deflagrations, and detonations. Stronger phase transitions with the same wall velocity have a larger value of v_p . Transitions with $v_p > v_w$ are forbidden as this would mean that in the wall frame fluid was flowing out from the bubble. We additionally colour each simulation point by the suppression factor in gravitational waves found in our study.

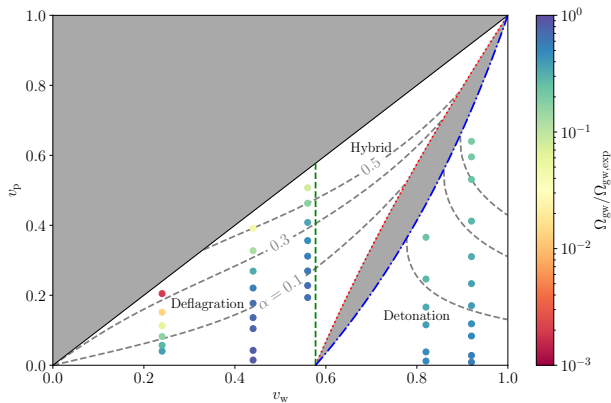


FIG. 9. Plot of maximum fluid flow velocity for the asymptotic profile v_p against the wall velocity. The green dashed line separates subsonic-deflagrations from supersonic-deflagrations. The blue dotted line gives the minimum v_p for a hybrid. Similarly the red dashed line shows the maximum v_p for a detonation. In the grey regions there are no solutions. See Fig. 7 of [58] for more details. Each point has been coloured according to the suppression in gravitational waves given in Table I. Lines of constant α are shown in dashed grey.

Evolution of global quantities

In Fig. 10 we plot how \bar{U}_f and \bar{U}_ϕ evolve for a deflagration and a detonation, both with strength $\alpha = 0.5$. We see that a rotational component of velocity \bar{v}_\perp is generated during the bubble collision phase, and that the deflagration generates \bar{v}_\perp more efficiently than the detonation. We also see that, for the deflagration, \bar{U}_ϕ de-

creases more slowly than it increases, indicating a slowing down of the phase boundary.

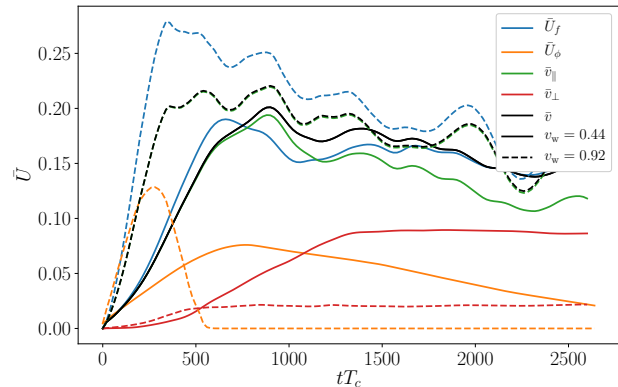


FIG. 10. The RMS fluid velocities decomposed into irrotational and rotational modes, plotted against time. We also plot the quantities \bar{U}_f and \bar{U}_ϕ . Solid lines show a subsonic deflagration with $\alpha = 0.5$, $v_w = 0.44$, and dashed lines a detonation with $\alpha = 0.5$, $v_w = 0.92$.

Simulation slice stills

In this supplemental material we include various stills taken from movies of our simulations of strong phase transitions in the early universe, which can be seen in Fig. 11 and Fig. 12. The movies these stills have been taken from can be found in a Vimeo album [57].

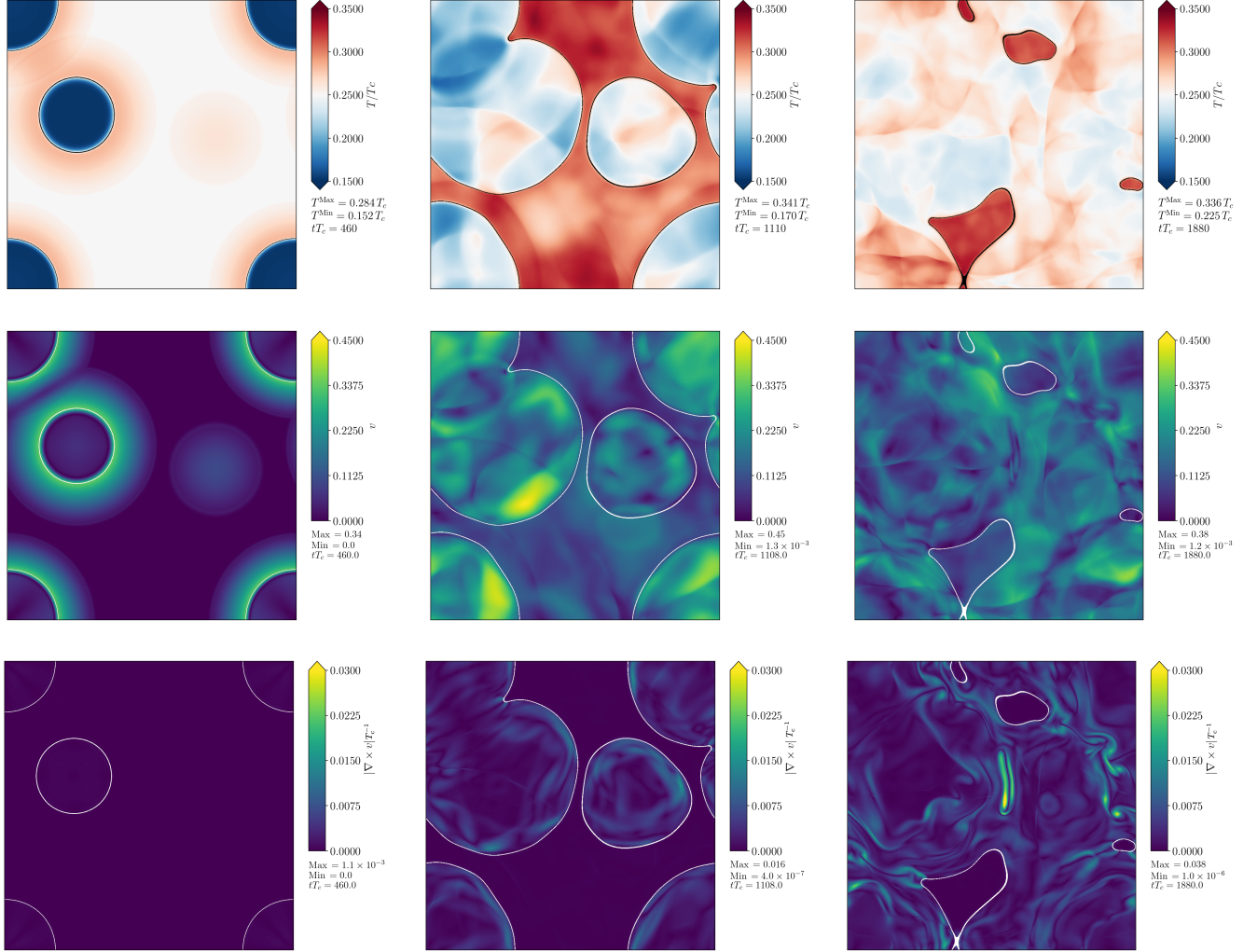


FIG. 11. Slices through $(0, y, z)$ for a simulation with $v_w = 0.44$, $\alpha = 0.5$, corresponding to a deflagration. In the top row we plot the temperature T/T_c . The midpoint of this colormap corresponds to T_n . The middle row shows the fluid velocity v . The bottom row shows the vorticity $|\nabla \times v|$. The bubble walls are shaded in black for the top row, and white for the middle and bottom row.

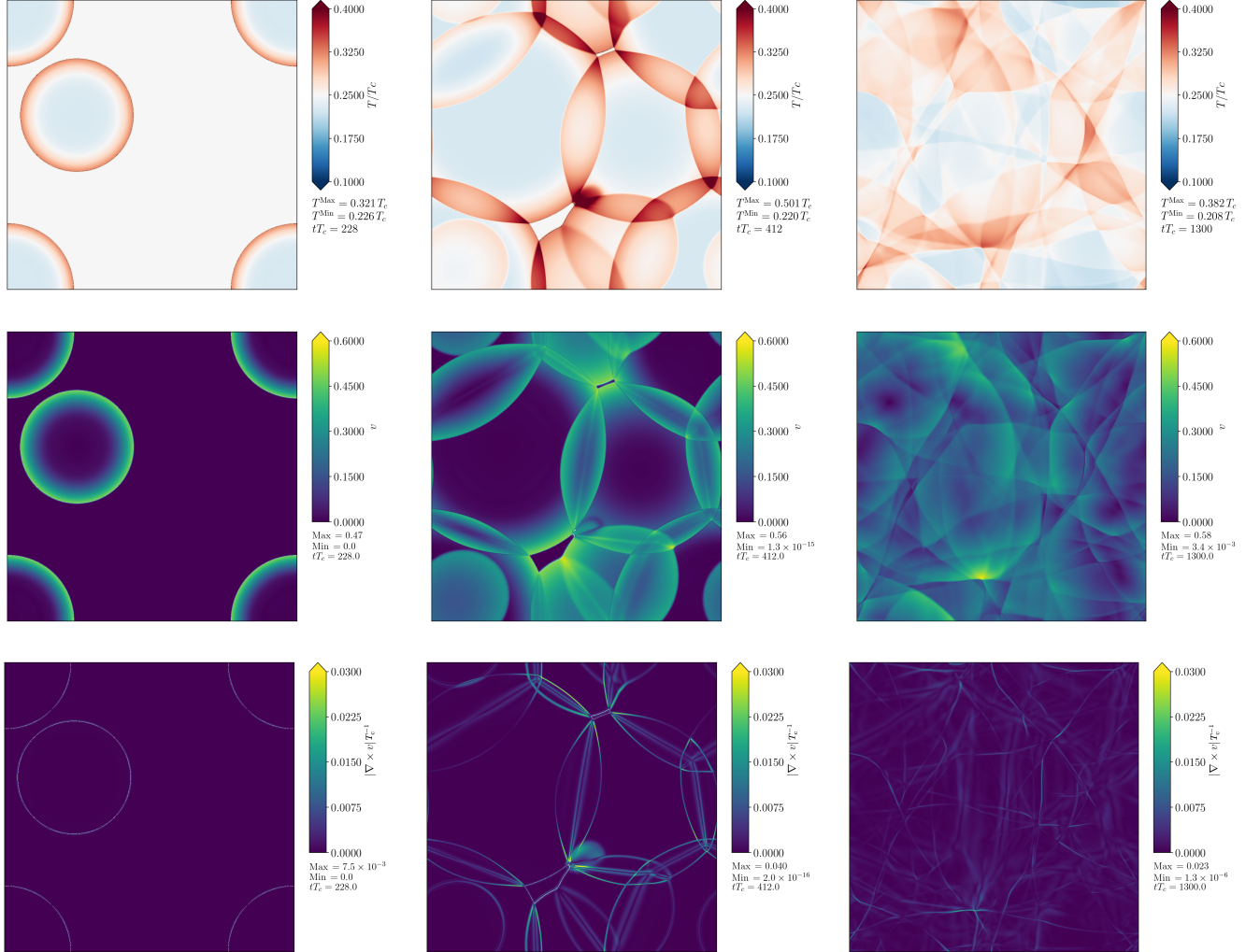


FIG. 12. Slices through $(0, y, z)$ for a simulation with $v_w = 0.92$, $\alpha = 0.5$, corresponding to a detonation. In the top row we plot the temperature T/T_c . The midpoint of this colormap corresponds to T_n . The middle row shows the fluid velocity v . The bottom row shows the vorticity $|\nabla \times v|$. The bubble walls are shaded in black for the top row, and white for the middle and bottom row.

Simulation parameters and measurements

v_w	α	T_n/T_c	$t_{\text{fin}}T_c$	η/T_c	$\bar{U}_{f,\text{max}}$	$\bar{U}_{f,\text{exp}}$	\bar{v}_\perp^2	\bar{v}^2	$\overline{\left(\frac{\Omega_{\text{gw}}}{H_n t}\right)} \frac{1}{H_n R_*}$	$\frac{\Omega_{\text{gw,exp}}}{H_n t} \frac{1}{H_n R_*}$
0.24	0.050	0.45	4.8×10^3	1.2	0.036	0.039	6.4×10^{-5}	1.3×10^{-3}	4.6×10^{-8}	1.2×10^{-7}
0.24	0.073	0.41	4.8×10^3	1.3	0.048	0.055	1.5×10^{-4}	2.3×10^{-3}	1.4×10^{-7}	5.0×10^{-7}
0.24	0.11	0.37	4.8×10^3	1.5	0.063	0.082	3.7×10^{-4}	4.1×10^{-3}	4.1×10^{-7}	2.4×10^{-6}
0.24	0.16	0.33	4.8×10^3	1.8	0.074	0.12	9.1×10^{-4}	5.7×10^{-3}	6.0×10^{-7}	9.5×10^{-6}
0.24	0.23	0.30	4.8×10^3	2.4	0.075	0.16	2.0×10^{-3}	5.9×10^{-3}	4.6×10^{-7}	3.3×10^{-5}
0.24	0.34	0.28	4.8×10^3	5.1	0.066	0.22	2.9×10^{-3}	4.4×10^{-3}	2.3×10^{-7}	1.2×10^{-4}
0.44	0.0050	0.79	2.4×10^3	0.34	0.0083	0.0069	1.7×10^{-7}	6.9×10^{-5}	1.0×10^{-10}	1.2×10^{-10}
0.44	0.016	0.59	2.4×10^3	0.52	0.025	0.021	1.4×10^{-6}	6.0×10^{-4}	9.1×10^{-9}	1.1×10^{-8}
0.44	0.050	0.45	2.4×10^3	0.66	0.066	0.061	1.6×10^{-5}	4.3×10^{-3}	5.6×10^{-7}	7.2×10^{-7}
0.44	0.073	0.41	2.4×10^3	0.71	0.090	0.085	4.0×10^{-5}	7.8×10^{-3}	2.0×10^{-6}	2.8×10^{-6}
0.44	0.11	0.37	2.4×10^3	0.81	0.12	0.12	1.1×10^{-4}	1.3×10^{-2}	7.0×10^{-6}	1.0×10^{-5}
0.44	0.16	0.33	2.4×10^3	0.94	0.15	0.16	3.0×10^{-4}	2.1×10^{-2}	2.0×10^{-5}	3.7×10^{-5}
0.44	0.23	0.30	2.4×10^3	1.2	0.18	0.22	1.0×10^{-3}	3.2×10^{-2}	4.3×10^{-5}	1.3×10^{-4}
0.44	0.34	0.28	2.4×10^3	1.7	0.18	0.30	3.6×10^{-3}	3.6×10^{-2}	5.2×10^{-5}	4.2×10^{-4}
0.44	0.50	0.25	2.4×10^3	3.5	0.19	0.39	8.0×10^{-3}	4.0×10^{-2}	5.8×10^{-5}	1.2×10^{-3}
0.56	0.050	0.45	2.8×10^3	0.53	0.080	0.075	1.3×10^{-5}	5.6×10^{-3}	1.1×10^{-6}	1.7×10^{-6}
0.56	0.073	0.41	2.8×10^3	0.59	0.10	0.10	3.5×10^{-5}	9.6×10^{-3}	3.6×10^{-6}	5.3×10^{-6}
0.56	0.11	0.37	2.8×10^3	0.67	0.14	0.14	9.2×10^{-5}	1.6×10^{-2}	1.2×10^{-5}	2.0×10^{-5}
0.56	0.16	0.33	2.8×10^3	0.76	0.18	0.19	2.4×10^{-4}	2.7×10^{-2}	3.6×10^{-5}	6.4×10^{-5}
0.56	0.23	0.30	2.8×10^3	0.90	0.22	0.25	5.8×10^{-4}	4.3×10^{-2}	9.3×10^{-5}	2.0×10^{-4}
0.56	0.34	0.28	2.8×10^3	1.2	0.27	0.33	1.5×10^{-3}	6.4×10^{-2}	2.1×10^{-4}	6.2×10^{-4}
0.56	0.50	0.25	2.8×10^3	1.7	0.28	0.43	5.2×10^{-3}	7.8×10^{-2}	3.1×10^{-4}	1.8×10^{-3}
0.56	0.67	0.23	2.8×10^3	2.9	0.30	0.51	1.1×10^{-2}	9.0×10^{-2}	3.0×10^{-4}	3.7×10^{-3}
0.82	0.0050	0.79	2.8×10^3	0.11	0.0064	0.0066	2.3×10^{-7}	4.0×10^{-5}	4.8×10^{-11}	1.0×10^{-10}
0.82	0.016	0.59	2.8×10^3	0.16	0.019	0.020	2.2×10^{-6}	3.6×10^{-4}	4.3×10^{-9}	9.1×10^{-9}
0.82	0.050	0.45	2.8×10^3	0.18	0.055	0.061	1.5×10^{-5}	2.8×10^{-3}	2.9×10^{-7}	7.6×10^{-7}
0.82	0.073	0.41	2.8×10^3	0.19	0.076	0.088	2.6×10^{-5}	5.2×10^{-3}	1.1×10^{-6}	3.2×10^{-6}
0.82	0.11	0.37	2.8×10^3	0.20	0.11	0.13	4.7×10^{-5}	9.4×10^{-3}	4.1×10^{-6}	1.4×10^{-5}
0.82	0.16	0.33	2.8×10^3	0.22	0.15	0.18	8.4×10^{-5}	1.6×10^{-2}	1.2×10^{-5}	5.5×10^{-5}
0.92	0.0050	0.79	2.4×10^3	0.053	0.0051	0.0051	3.2×10^{-7}	2.6×10^{-5}	2.0×10^{-11}	3.6×10^{-11}
0.92	0.016	0.59	2.4×10^3	0.086	0.015	0.016	3.4×10^{-6}	2.4×10^{-4}	1.9×10^{-9}	3.6×10^{-9}
0.92	0.050	0.45	2.4×10^3	0.099	0.045	0.049	2.2×10^{-5}	1.9×10^{-3}	1.5×10^{-7}	3.0×10^{-7}
0.92	0.073	0.41	2.4×10^3	0.10	0.064	0.070	3.6×10^{-5}	3.7×10^{-3}	6.0×10^{-7}	1.3×10^{-6}
0.92	0.11	0.37	2.4×10^3	0.10	0.087	0.10	5.8×10^{-5}	6.9×10^{-3}	2.4×10^{-6}	6.0×10^{-6}
0.92	0.16	0.33	2.4×10^3	0.11	0.12	0.14	8.8×10^{-5}	1.2×10^{-2}	8.4×10^{-6}	2.3×10^{-5}
0.92	0.23	0.30	2.4×10^3	0.11	0.16	0.20	1.4×10^{-4}	2.0×10^{-2}	2.6×10^{-5}	8.0×10^{-5}
0.92	0.34	0.28	2.4×10^3	0.12	0.21	0.27	2.5×10^{-4}	3.2×10^{-2}	8.1×10^{-5}	2.9×10^{-4}
0.92	0.50	0.25	2.4×10^3	0.13	0.28	0.36	4.6×10^{-4}	4.9×10^{-2}	2.2×10^{-4}	9.3×10^{-4}
0.92	0.60	0.24	2.4×10^3	0.14	0.32	0.42	6.3×10^{-4}	5.8×10^{-2}	3.5×10^{-4}	1.6×10^{-3}
0.92	0.67	0.23	2.4×10^3	0.15	0.34	0.45	7.8×10^{-4}	6.5×10^{-2}	4.5×10^{-4}	2.2×10^{-3}

TABLE I. Key simulation parameters and measured quantities used to generate the graphs in this paper. Note that $\overline{\left(\frac{\Omega_{\text{gw}}}{H_n t}\right)}$ signifies that we average the quantity inside the brackets over the final $\Delta t = 2R_*$ of the simulation.